Supporting Information for:

Dramatic changes in Harbin aerosol during 2018–2020: the roles of open burning policy and secondary aerosol formation

Yuan Cheng[1], Qin-qin Yu[1], Jiu-meng Liu[1,*], Xu-bing Cao[1], Ying-jie Zhong[1], Zhen-yu Du[2], Lin-lin Liang[3], Guan-nan Geng[4], Wan-li Ma[1], Hong Qi[1], Qiang Zhang[5], Ke-bin He[4]

[1] State Key Laboratory of Urban Water Resource and Environment, School of Environment, Harbin Institute of Technology, Harbin, China

[2] National Research Center for Environmental Analysis and Measurement, Environmental Development Center of the Ministry of Ecology and Environment, Beijing, China

[3] State Key Laboratory of Severe Weather & CMA Key Laboratory of Atmospheric Chemistry, Chinese Academy of Meteorological Sciences, Beijing, China

[4] State Key Joint Laboratory of Environment Simulation and Pollution Control, School of Environment, Tsinghua University, Beijing, China

[5] Department of Earth System Science, Tsinghua University, Beijing, China

[*] Corresponding author. Jiu-meng Liu (jiumengliu@hit.edu.cn).

SI-1. Field observation.

Two campaigns were conducted at an urban site in Harbin during the heating seasons of 2018–2019 (from 16 October, 2018 to 14 April, 2019; N = 180) and 2019–2020 (from 16 October, 2019 to 4 February, 2020; N = 112). The sampling was performed in the campus of Harbin Institute of Technology (45°45′24″ N, 126°40′49″ E), using a low volume sampler (MiniVol; Airmetrics, OR, USA) operated with pre-baked quartz-fiber filters (2500 QAT-UP; Pall Corporation, NY, USA) at a flow rate of 5 L/min. As described in Cheng et al. (2021), the samples were analyzed for organic carbon (OC), elemental carbon (EC), organic tracers for biomass burning (levoglucosan and mannosan) and water-soluble inorganic ions. Briefly, OC and EC were measured by a thermal/optical carbon analyzer (DRI-2001; Atmoslytic Inc., CA, USA), using the IMPROVE-A temperature protocol with transmittance charring correction. Levoglucosan and mannosan were detected by a Dionex ion chromatography (IC) system (ICS-5000$^+$; Thermo Fisher Scientific Inc., MA, USA), using the high-performance anion-exchange chromatography coupled to pulsed amperometric detection (HPAEC-PAD) method. The IC was also used to determine the inorganic ions including sulfate, nitrate, ammonium, etc.

Hourly air quality data (e.g., CO), which were measured at a nearby monitoring site (Taiping Hongwei Park, about 2.4 km away from the filter sampling site) operated by the China National Environmental Monitoring Center (CNEMC), were obtained from China's National Urban Air Quality Real Time Publishing Platform (http://106.37.208.233:20035/). Hourly meteorological data including temperature and relative humidity were obtained from Weather Underground (https://www.wunderground.com).

SI-2. Aerosol water content (AWC) and aerosol pH estimated using ISORROPIA-II

To estimate AWC and aerosol pH during the two campaigns, ISORROPIA-II was run with daily-integrated data (including concentrations of aerosol-phase species, ambient temperature and relative humidity) as input. To simplify the simulations, ISORROPIA-II was run assuming particles are "metastable". It is also assumed that the particles are internally mixed and that pH does not vary with particle size (so that bulk properties represent the overall aerosol pH).

Because of limitations in input data, e.g., no gas phase data available directly on site, the calculation was done in two ways, the "reverse" and "forward" mode. For the "reverse" mode, the measured aerosol-phase data were deployed as input to retrieve AWC and pH directly. For the "forward" mode, the model was run in an "iteration" way, that we used the measured aerosol-phase data as initial input, ran ISORROPIA-II in the "forward" mode to predict gas-phase concentrations of NH_3, HNO_3 and HCl, and used the sum of predicted gas-phase and measured aerosol-phase

concentrations as the input for next round. The calculations were repeated until the simulated results were stable and in line with the observational data. Both the reverse and forward modes showed comparable AWC levels (Figure S14). For pH, we specifically deployed results using the forward mode, as studies have suggested that the forward mode gives more accurate and robust results than the reverse mode (e.g., Guo et al., 2017, 2018; Song et al., 2018).

References

Cheng, Y., Yu, Q. Q., Liu, J. M., Du, Z. Y., Liang, L. L., Geng, G. N., Zheng, B., Ma, W. L., Qi, H., Zhang, Q., and He, K.B.: Strong biomass burning contribution to ambient aerosol during heating season in a megacity in Northeast China: effectiveness of agricultural fire bans?, ***Sci. Total Environ.***, 754, 142144, 2021.

Guo, H. Y., Liu, J. M., Froyd, K. D., Roberts, J. M., Veres, P. R., Hayes, P. L., Jimenez, J. L., Nenes, A., and Weber, R. J.: Fine particle pH and gas–particle phase partitioning of inorganic species in Pasadena, California, during the 2010 CalNex campaign, ***Atmos. Chem. Phys.***, 17, 5703–5719, 2017.

Guo, H. Y., Otjes, R., Schlag, P., Kiendler-Scharr, A., Nenes, A., and Weber, R. J.: Effectiveness of ammonia reduction on control of fine particle nitrate, ***Atmos. Chem. Phys.***, 18, 12241–12256, 2018

Song, S. J., Gao, M., Xu, W. Q., Shao, J. Y., Shi, G. L., Wang, S. X., Wang, Y. X., Sun, Y. L., and McElroy, M. B.: Fine-particle pH for Beijing winter haze as inferred from different thermodynamic equilibrium models, ***Atmos. Chem. Phys.***, 18, 7423–7438, 2018.

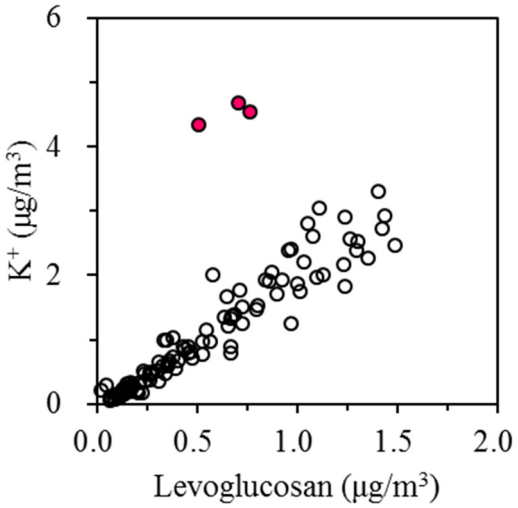

Figure S1. Relationship between K^+ and levoglucosan during the 2019–2020 campaign. Three samples collected during the Chinese New Year period exhibit substantially higher K^+ to levoglucosan ratios (as highlighted by the solid circles), pointing to significant influence of firework emissions.

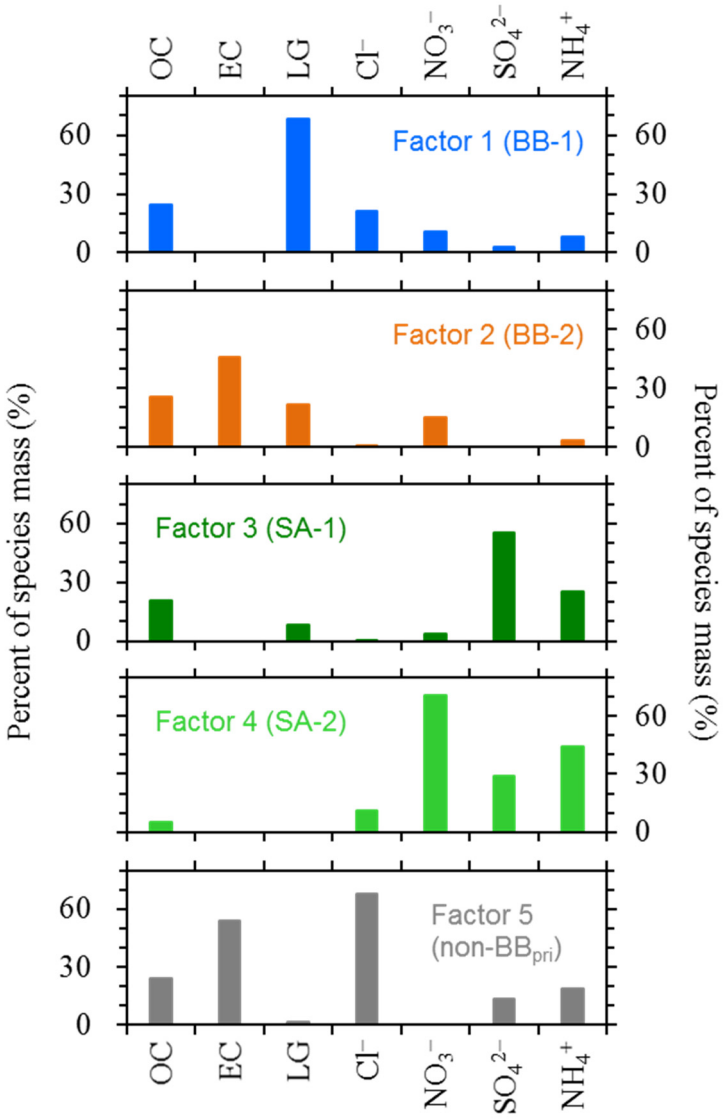

Figure S2. Source profiles resolved by PMF.

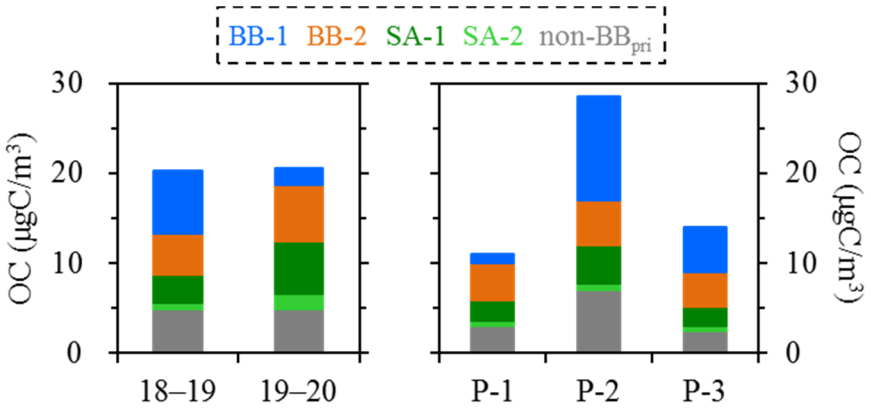

Figure S3. Comparisons of OC source apportionment results between the 2018–2019 and 2019–2020 campaigns (left panel), and across the 2018–2019 samples collected before (P-1), during (P-2) and after (P-3) the "legitimate burning" periods (right panel).

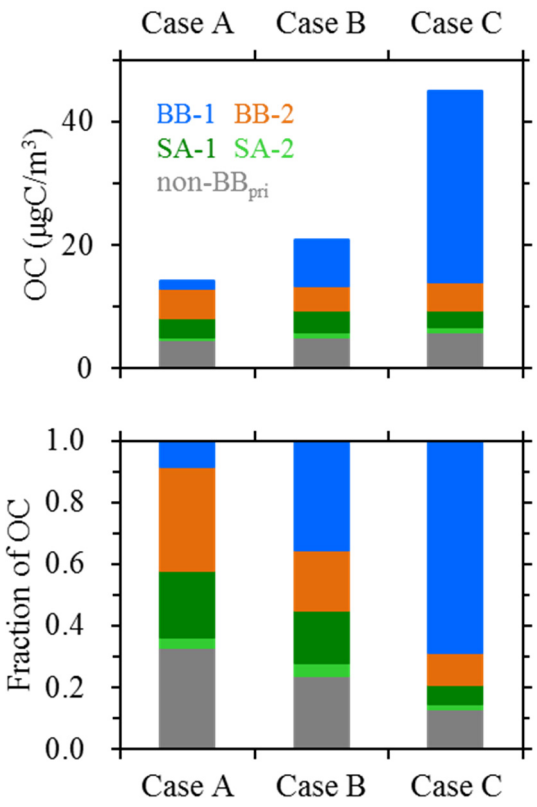

Figure S4. Comparison of OC source apportionment results across the 2018–2019 samples with increasing strength of biomass burning impacts. Cases A, B and C correspond to LG/OC ranges of < 1.5%, 1.5–3.0% and > 3.0%, respectively.

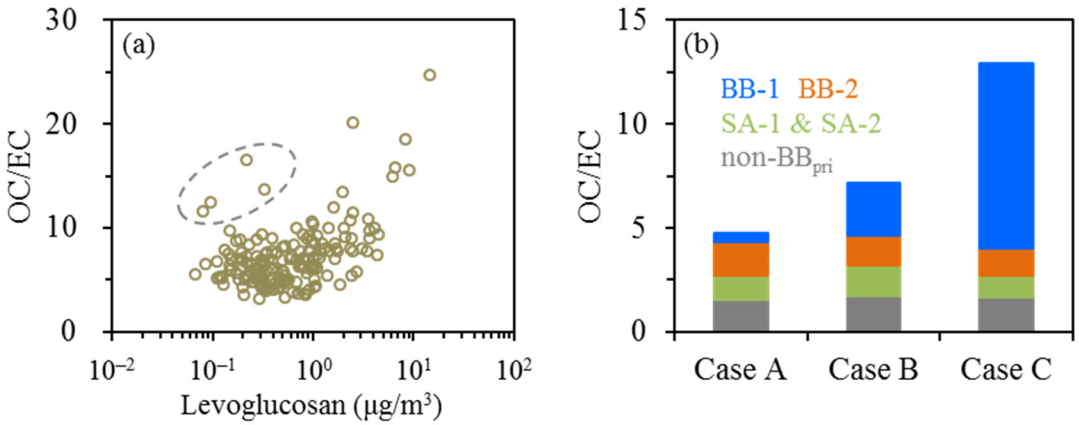

Figure S5. (a) Relationship between OC/EC and levoglucosan, and **(b)** comparison of OC/EC among Cases A–C, for the 2018–2019 campaign. OC/EC ratios in (b) are based on results from PMF analysis, i.e., for each case, OC/EC is presented as the sum of source-resolved OC to total EC ratios (e.g., $OC_{BB\text{-}1}$/EC and $OC_{BB\text{-}2}$/EC). The two factors representing secondary aerosols are not distinguished in (b). In general, OC/EC showed a positive dependence on levoglucosan, although there appeared to be several outliers (as highlighted by the dashed oval) which had the lowest EC concentrations of the measurement period (below ~0.5 μg/m^3). Thus, biomass burning is considered the dominant driver for the temporal variation of OC/EC during the 2018–2019 campaign. This inference is also supported by (b), as OC/EC exhibited an increasing trend from Case A through Case C, which cannot be explained by SOA or non-BB emissions.

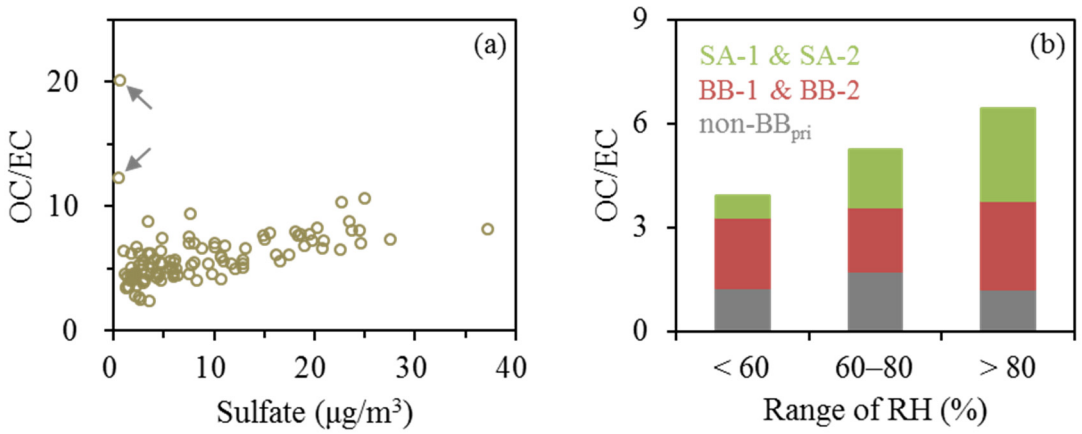

Figure S6. (a) Relationship between OC/EC, and **(b)** comparison of OC/EC with increasing RH levels, for the 2019–2020 campaign. In general, OC/EC showed a positive dependence on sulfate, although there were two outliers (as highlighted by the arrows) which had the lowest EC concentrations of the measurement period (below 0.3 μg/m^3). Thus, SOA is considered the dominant driver for the temporal variation of OC/EC during the 2019–2020 campaign. This inference is also supported by (b), as with increasing RH, OC/EC exhibited an increasing trend, which cannot be explained by the primary factors (either BB or non-BB).

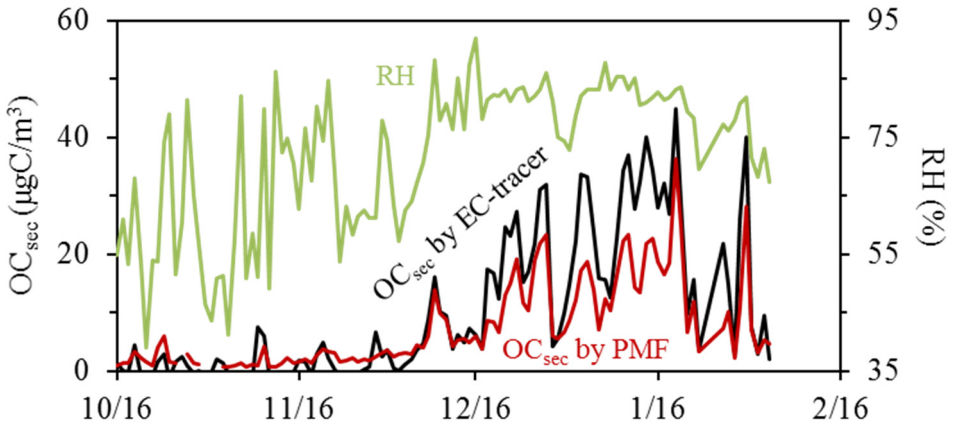

Figure S7. Temporal variations of OC_{sec} and RH during the 2019–2020 campaign. The PMF-based OC_{sec} was calculated as the sum of OC masses attributed to the SA-1 and SA-2 factors. For the EC-tracer method, OC_{sec} was calculated as: $OC_{sec} = OC - EC \times (OC/EC)_{pri} - OC^*$, where $(OC/EC)_{pri}$ is the OC to EC ratio representative of combustion sources and OC^* indicates primary OC from non-combustion sources. For the 2019–2020 campaign, $(OC/EC)_{pri}$ and OC^* were determined as the slope (2.13) and intercept (3.11) from the linear regression of OC on EC (r = 0.98), respectively, based on the low-RH samples (i.e., those with RH below 60%). Compared to the PMF-based results, OC_{sec} calculated by the EC-tracer method showed a similar pattern of temporal variation. Results from both methods showed RH-dependent increase of OC_{sec}.

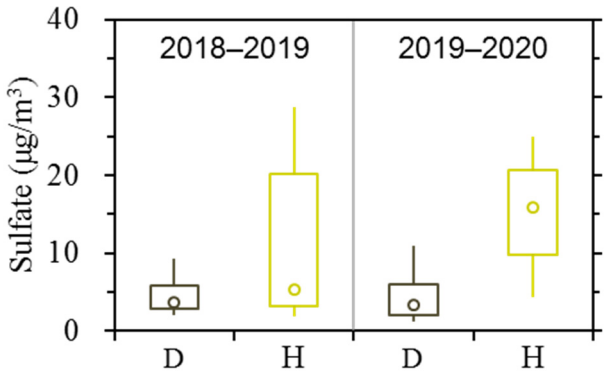

Figure S8. Comparison of sulfate between different RH levels for the 2018–2019 and 2019–2020 campaigns. The terms "D" and "H" indicate relatively dry and more humid conditions with RH below and above 80%, respectively.

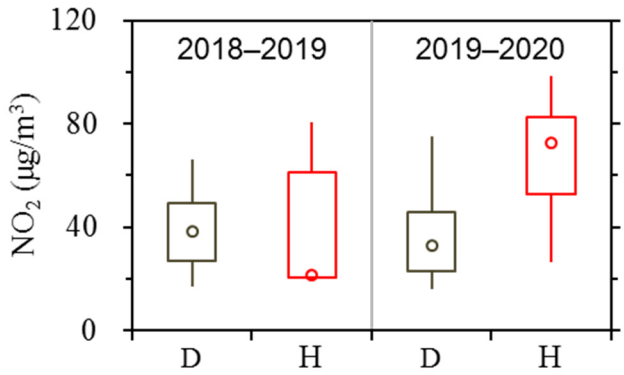

Figure S9. Comparison of NO_2 between different RH levels for the 2018–2019 and 2019–2020 campaigns. The terms "D" and "H" indicate relatively dry and more humid conditions with RH below and above 80%, respectively.

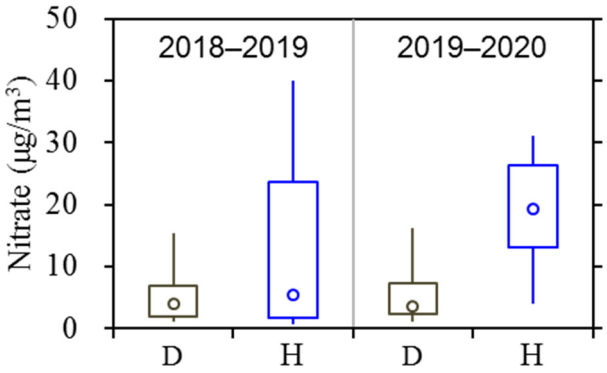

Figure S10. Comparison of nitrate between different RH levels for the 2018–2019 and 2019–2020 campaigns. The terms "D" and "H" indicate relatively dry and more humid conditions with RH below and above 80%, respectively.

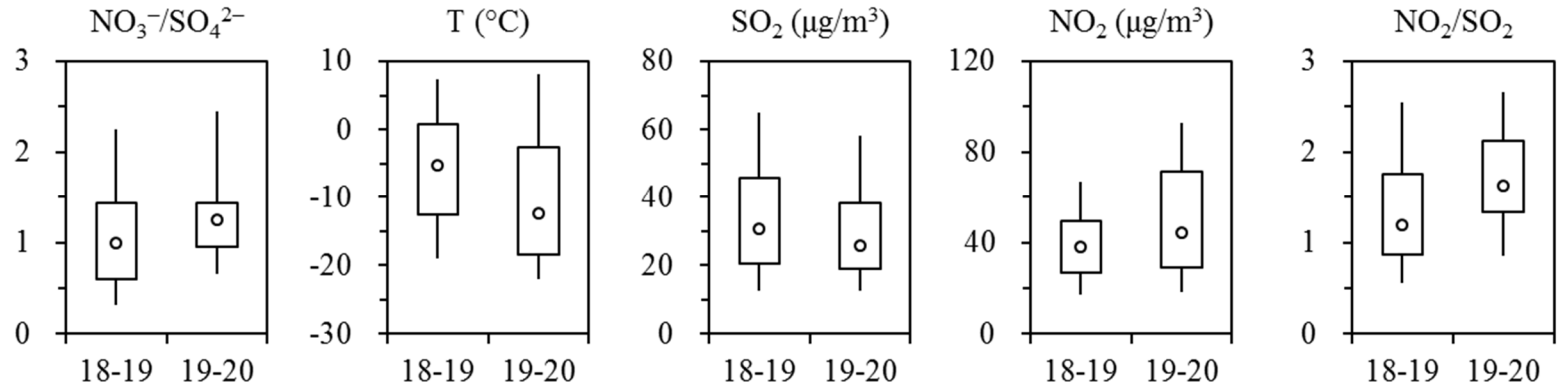

Figure S11. Comparisons of the nitrate to sulfate ratios, temperature, SO_2, NO_2 and the NO_2 to SO_2 ratios between the 2018–2019 and 2019–2020 campaigns.

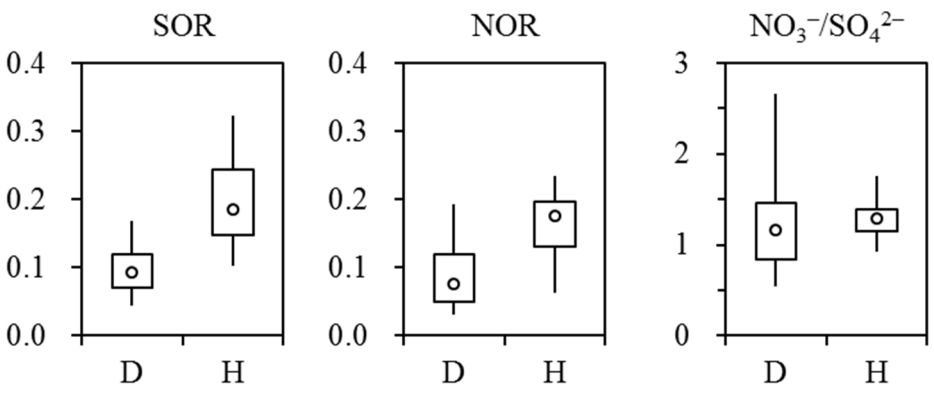

Figure S12. Comparisons of SOR, NOR and the nitrate to sulfate ratios at different RH levels for the 2019–2020 campaign.

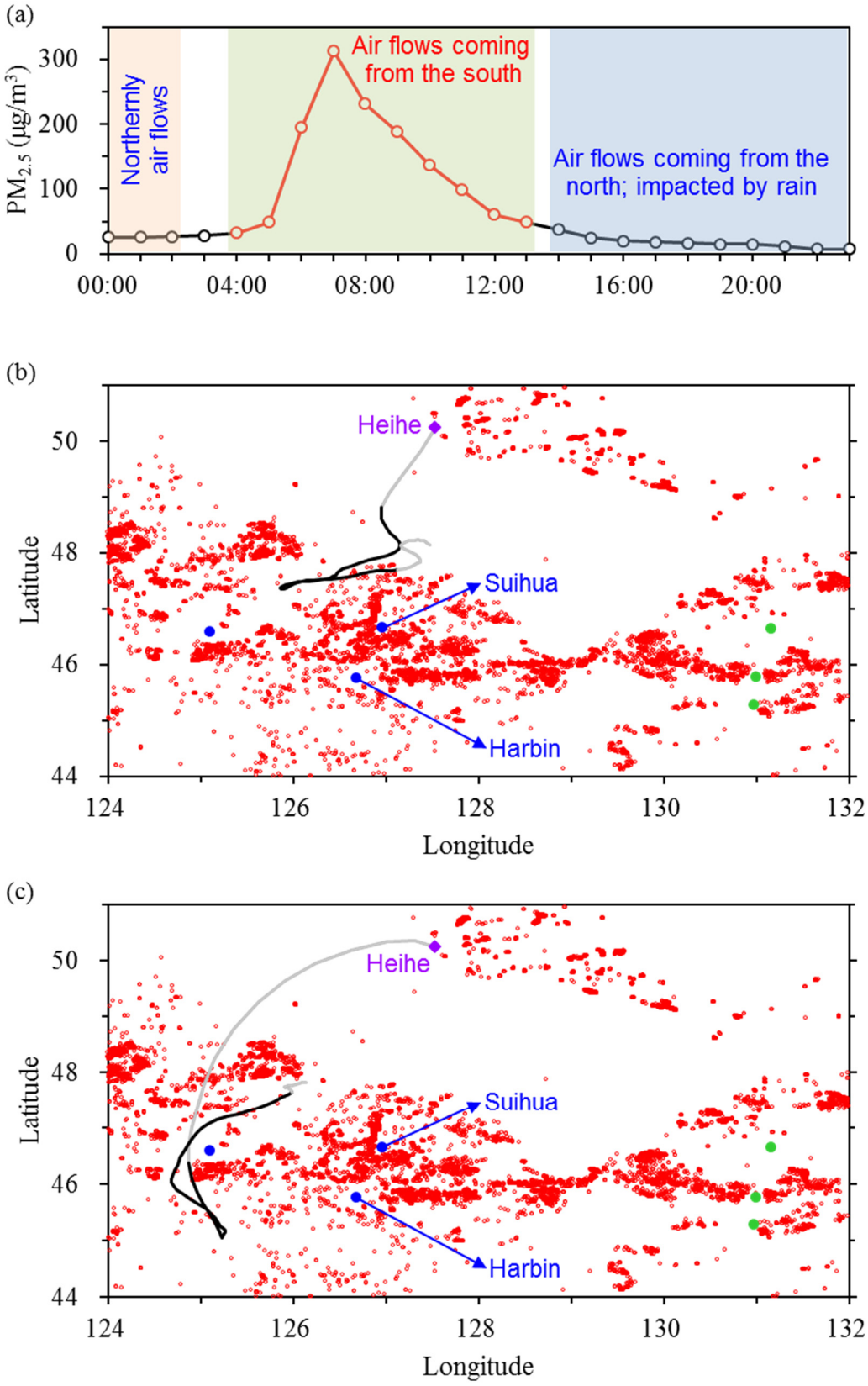

Figure S13. (a) Temporal variation of 1-h $PM_{2.5}$ observed in Heihe on 19 April, 2020. **(b–c)** 72-hour back trajectories ending at 4:00 and 13:00, respectively, in Heihe, overlaid with active fires detected during 17–18 April, 2020 as red circles. $PM_{2.5}$ were relatively low between 0:00 and 3:00,

when the air flows came from the northwest, moved fast and descended sharply. $PM_{2.5}$ started to increase at 4:00, with the trajectory from the south and impacted by the region with agricultural fires (as shown in b). The increase of $PM_{2.5}$ continued as the trajectory path moved towards Harbin and Suihua, where the impacts of open burning were inferred to be extremely strong based on their off-the-chart $PM_{2.5}$ concentrations. The maximum $PM_{2.5}$ was observed at 7:00, and then $PM_{2.5}$ started to decrease although the air masses still passed over the Harbin-Suihua region (or the nearby area) before arriving at Heihe. A likely cause for the decrease of $PM_{2.5}$ after 7:00 was the increase of planetary boundary layer height from morning through noon time. The trajectory left the Harbin-Suihua region at 13:00 (as shown in c) and returned to the north at 14:00. In addition, there was rain in Heihe after 14:00, and correspondingly, $PM_{2.5}$ gradually decreased to below 10 $\mu g/m^3$.

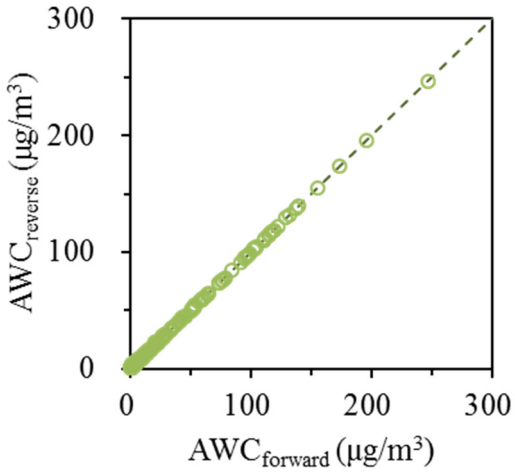

Figure S14. Comparison of AWC results predicted by reverse and forward modes. The dashed line indicates one-to-one correspondence.